Journal of Materials Chemistry A

PAPER

View Article Online
View Journal | View Issue

Cite this: J. Mater. Chem. A, 2018, 6, 21475

Safety issues caused by internal short circuits in lithium-ion batteries†

Binghe Liu,‡[ab] Yikai Jia,‡[ab] Juan Li,[c] Sha Yin,[ab] Chunhao Yuan,[ab] Zihan Hu,[ab] Lubing Wang,[ab] Yangxing Li*[c] and Jun Xu*[ab]

Safety related incidents and accidents involving lithium-ion batteries (LIBs) are often in the news. Even though catastrophic failure is rare, the high socioeconomic risks associated with battery thermal runaway reactions cannot be overlooked, as demonstrated by recent high-profile events. Among all the known types of battery failure modes, the internal short circuit (ISC) tops the list of the major safety concerns for the lithium-ion battery. However, a clear picture of the LIB's electrochemical safety behavior in the context of the ISC remains to be fully established. Herein we show that mechanical indentation techniques are capable of producing highly repeatable and controllable ISC modes in a manner that allows the electrochemical safety behavior of LIBs to be categorized based on the state of charge (SOC), ISC resistance, and electrode area. Our results identify the fundamental mechanism(s) of various electrochemical responses to the ISC through a combination of experiment, numerical simulation, and analysis. With the understanding that complicated electrochemical phenomena occur after the triggering of an ISC, we examine the safety boundaries and create an electrochemical behavior map for LIBs after ISCs. We anticipate that this discovery will lead to new opportunities for battery safety design, manufacturing, monitoring, and utilization with beneficial consequences to a battery-intensive, mobile, and green society in terms of much reduced battery safety concerns.

Received 15th September 2018
Accepted 1st October 2018

DOI: 10.1039/c8ta08997c

rsc.li/materials-a

1. Introduction

Currently, there are more than 2 million electric vehicles in operation on the road with lithium-ion battery capacities in the 20–90 kW h range and more than 7 billion cellphones in active use worldwide with battery capacities ranging from 1700 to 4000 mA h. Battery safety has attracted intensive attention globally due to current trends in communication and mobilization brought about by rapidly evolving versions of the smart phone, tablet, laptop, and other electronic devices, and the persistent increase in the number of electric vehicles.[1–4]

One of the fast-growing concerns in hazardous event scenarios for LIBs involves events triggered by the inevitable occurrence of mechanical deformation, crushing, and penetration.[5,6] In particular, during the mechanical loading process, LIBs may experience mechanical deformation leading to an ISC that evolves into a thermal runaway (TR). This process involves a transient series of mechanical, thermal, and electrochemical events that evolve with time in a complex manner that has prevented deeper understanding of LIB failure modes. A schematic diagram illustrating the physical and chemical processes occurring during a lithium-ion battery ISC event is shown in Extended Data Fig. S1.† A number of previous studies that focused on the processes outlined in Fig. S1† have attempted to (1) suggest various ways to trigger an ISC, including thermal,[7–10] electrical[11–14] and mechanically-forced[15–17] methods and (2) investigate the electrochemical and thermal behaviour of LIBs after an ISC.[18–20]

Plenty of experimental methods have been developed to trigger an ISC. For the thermally triggered method, there are phase change material methods developed by the National Renewable Energy Laboratory (NREL) and NASA,[7] and the memory alloy method proposed by Ouyang's group.[21] For the electrically triggered method, fast charge/discharge over charging/discharging and cycling can cause an ISC. To control the ISC position, a metallic particle is retrofitted into the battery.[22] For the mechanically triggered method, penetration,[23] pre-holed separator methods[24,25] and internal particles[18] are all popular superficial ISC trigger methods. Herein we describe a mechanical indentation loading technique that allows us to initiate an ISC in a LIB cell in a highly repeatable and controllable ISC modes way. Combined with experiment, numerical simulation, and analysis, our results identify the fundamental mechanism(s) of various electrochemical responses to an ISC. With the understanding that complicated electrochemical

[a]Department of Automotive Engineering, School of Transportation Science and Engineering, Beihang University, Beijing, 100191, China. E-mail: junxu@buaa.edu.cn
[b]Advanced Vehicle Research Center (AVRC), Beihang University, Beijing, 100191, China
[c]Central Research Institute, Huawei Technologies Co., LTD, Longgang District, Shenzhen, 518129, China. E-mail: li.yangxing@huawei.com

† Electronic supplementary information (ESI) available. See DOI: 10.1039/c8ta08997c

‡ These authors have contributed equally.

phenomena occur after the triggering of an ISC, we examine the safety boundaries and create an electrochemical behaviour map for LIBs after ISCs.

The electrochemical and thermal behaviour of LIBs after an ISC is complex and random. Evidence has shown that the ISC types (*e.g.* anode–cathode, anode–current collector, cathode–current collector and current collector–current collector types),[18] mechanical stress[26] and material melting[27] can all affect the ISC process. Due to these reasons, the absence of reproducible testing methods and the difficulties associated with observing the evolution of internal material chemistry and structural transformation have provided much of the understanding of the fundamental mechanism(s) of superficial ISC-to-TR. Herein we describe a mechanical indentation loading technique that allows us to initiate an ISC in a LIB cell in a highly repeatable and controllable ISC mode way. Combined with experiment, numerical simulation, and analysis, our results identify the fundamental mechanism(s) of various electrochemical responses to an ISC. With the understanding that complicated electrochemical phenomena occur after the triggering of an ISC, we examine the safety boundaries and create an electrochemical behaviour map for LIBs after ISCs.

2. Experimental

2.1. Penetration test

The experimental equipment is shown in Fig. 1a and Table S1.† The battery samples were supplied by HUAWEI company and charged to the denoted SOC value by the BK6808AR rechargeable battery performance testing equipment with a controlling computer. Then, batteries were placed on the compression test platform (110 mm diameter), and two electrodes were connected to an Agilent 34410A digital voltmeter (as shown in Fig. 1b). The LIB surface temperature was measured *in situ* by ANBAI AT4508 multi-channel temperature sensors and K-type thermocouples. The platform was installed on an INSTRON 8801 universal material testing machine. At the same time, the phenomenon of the experiment was recorded using a camera.

A steel particle with a 2 mm diameter was placed in the center of the geometry of a battery (as shown in Fig. 1b and c). When the experiment was carried out, the platform moved up and squeezed the foreign matter into the battery.

In the meantime, the cell voltage and potentials for both cathode and anode variations with the SOC are also demonstrated in Fig. 1d and e, providing a clear picture of the electrochemical status of cells with various SOC values in our study.

2.2. Contact resistance measurement experiment

An INSTRON 2345 universal material testing machine was used as the mechanical testing platform for tests. The contact resistance was measured using an Agilent 34420A digital voltmeter.

Short-circuit resistance of all four contact forms was measured, *i.e.*, (I) An–Ca, (II) Ca–Cu, (III) An–Al, and (IV) Al–Cu (as shown in Fig. 2a). According to the corresponding combination forms, these samples were placed on the compression test platform and two electrodes were connected to the digital voltmeter (as shown in Fig. 2b and c). The battery electrode samples were cut into rectangle shapes with 80 mm length and 50 mm width. The contact area is a circle with a 10 mm diameter. In the contact region, the active material was shaved off and lost a hole in the diaphragm (as shown in Fig. 2d). The active material in the sensor connection area was shaved off. During the experiment, the press head moved down to contact the electrode. The relation between the contact force and contact resistance is determined.

3. Simulation methods

3.1. Modelling and calibrating the finite element (FE) model of an LIB

A detailed FE model was built in this paper, consisting of a cover, anode, cathode, separator and current collector as shown in Fig. 3a. The geometry and material parameters of the LIB are shown in Table S2.†

The material of the separator is PE ceramic coating, and there are no obvious anisotropic properties as determined through the tension experiment. The material of the cover is an aluminium plastic film with no anisotropic properties. Thus an elasto-plastic model is used for these two materials. The shear element is used for the battery cover, while the solid element is used for the separator.

A one-layer cathode/anode is a sandwich structure consisting of a middle Al/Cu shell and the outer porous $LiCoO_2$/LiC_x. The elasto-plastic model is used for the Al/Cu shell while the crushable foam model is used for porous $LiCoO_2$/LiC_x. A one-layer shell (current collector) with a two-layer-solid (active materials) method is used to simulate the anode and cathode; the shell and the solid share the same nodes in the contact surface as shown in Fig. 3a. A penalty contact method is used for other contact surfaces.

Both tension and compression tests were setup to calibrate the cathode/anode model. 5 mm × 60 mm rectangular specimens of the cathode/anode with a current collector are chosen for tension tests while 20 stake layer wafers with a radius of 8 mm were chosen for compression. An INSTRON 8801 with a maximum loading of 100 kN and an INSTRON 2345 with a maximum loading of 5000 N were used for compression and tension tests separately due to different load ranges. As shown in Fig. S4a–d†, both compression and tension tests can calibrate well with the simulation results of cathode/anode models.

Tension tests were setup for calibrating separator and cover models. A 5 mm × 60 mm rectangular specimen of the cover and separator were chosen for tension tests. As shown in Fig. S4e and f,† the tension tests can calibrate well with the simulation results.

The FE model was used to predict the mechanical behaviour of the penetration test. In the simulation setups, the platform is fixed and the indenter is given forced displacement. Fig. 3b shows the calibration results and it proved that the FE predicts well under particle penetration.

3.2. Multi-physics method of the LIB

The multi-physics model of the LIB consists of a total of 5 sub models (*e.g.* mechanical model, thermal model, short-circuit

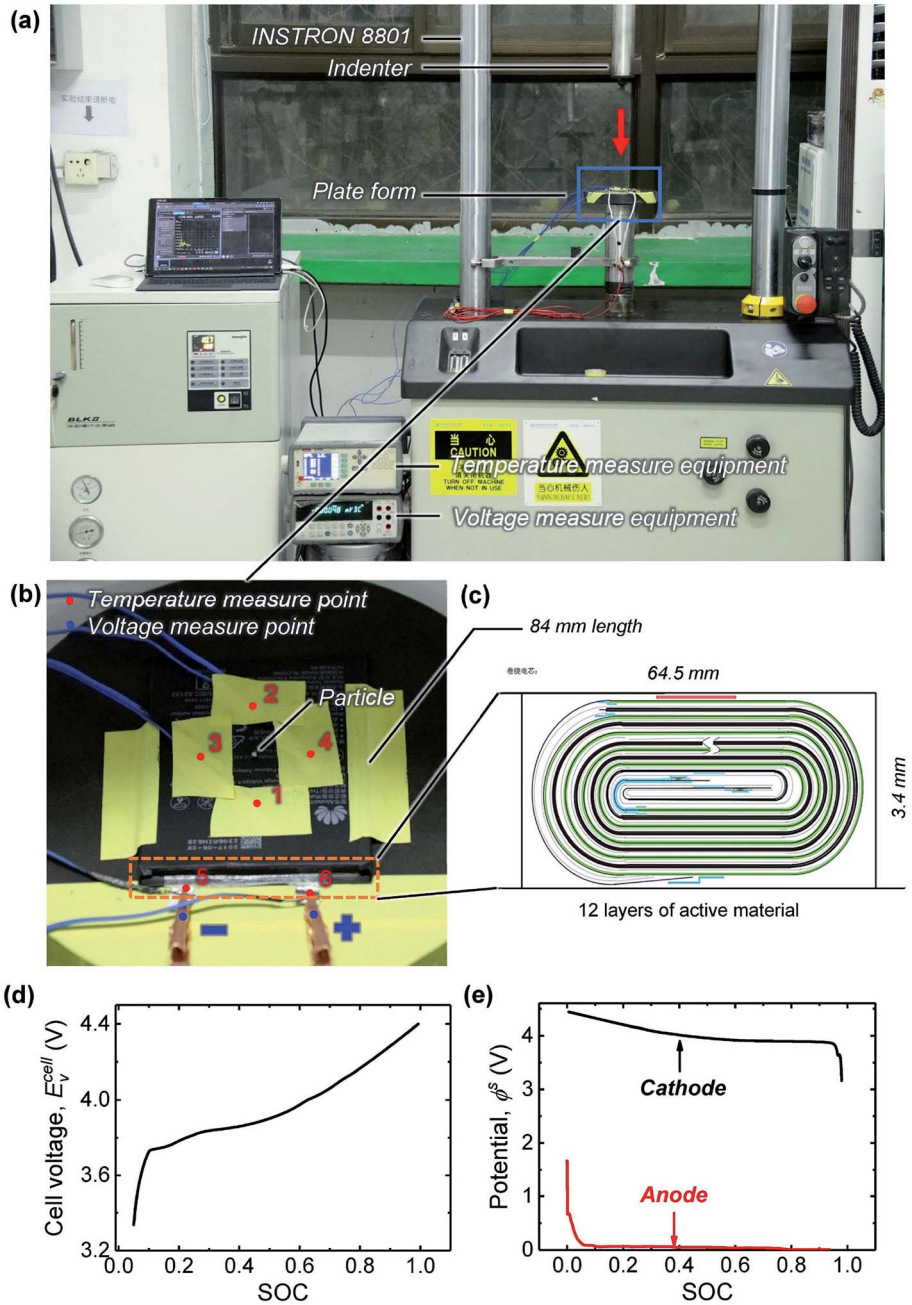

Fig. 1 Design of the penetration experiment for an LIB: (a) testing equipment illustration, (b) experimental platform and sensor measurement point indication, and (c) construction and geometrical information of a prismatic pouch cell. (d) Cell voltage change with the SOC variation and (e) potential change for various SOCs for the cathode and anode, respectively.

model, battery model and thermal runaway model as shown in Fig. 3c) to describe the short-circuit behaviour. The main equation of those models has been described in Table. S3.†

A single particle battery model is used to compute the voltage drop and heat produced; the charge/discharge characteristic curve is shown in Fig. S3.† The mechanical model with homogenized material properties of components is used to compute the mechanical stress and deformation field under ISC conditions. The ISC model is built to calibrate the ISC resistance, ISC position and heat produced. The thermal runaway model is used to calculate the heat caused by a thermal runaway. Note that, the thermal runaway model only considers the main chemical reactions (SEI decomposition, anode–electrolyte reaction, cathode–electrolyte reaction and electrolyte decomposition[28]) for necessary simplification. The thermal model is also used to calculate the heat transfer. The geometric boundary of the thermal model is determined by the mechanical model.

The trigger of an ISC can be determined by the mechanical stress.[15] The critical stress σ_c can be set for an ISC criterial.

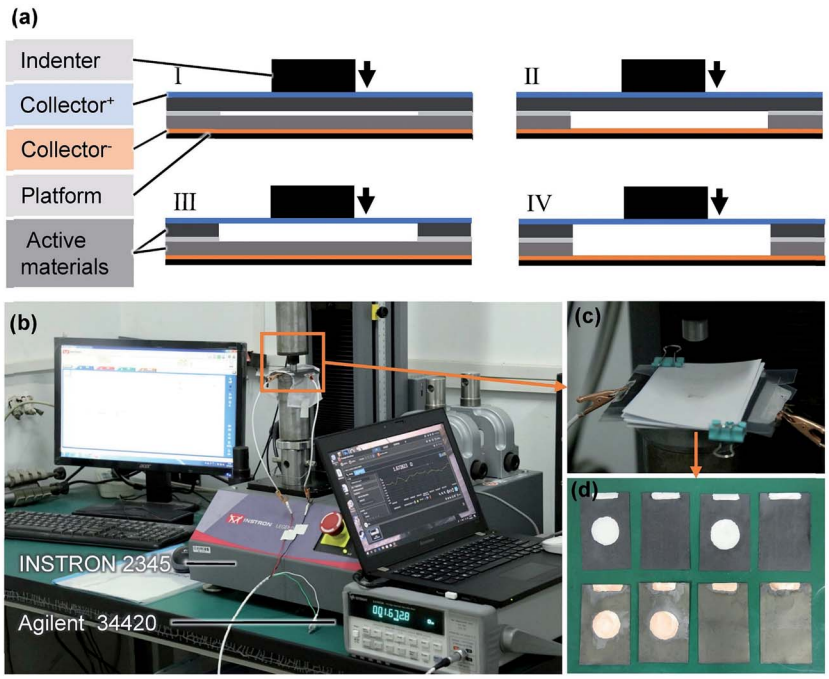

Fig. 2 Measurement of electrode contact resistance. (a) Four types of contact, (b) experimental equipment diagram (c) experimental situation diagram, and (d) test samples.

Considering the four types of ISC modes that occur at the same time, the initial ISC resistance is assumed by equivalent electrical conductivity after the ISC is triggered. After the ISC triggered, the separator and current collector melting lead to the change of ISC resistance in a specific location. The Arrhenius equation is used to predict the melting phenomenon. The melting of the current collector (Cu/Al) will increase the resistance while the melting of the separator will produce a new short-circuit contact; thus the relationship of electrical conductivity and the melting state can be assumed in the functions.

4. Results and discussion

Typical relationships among mechanical loading, voltage and temperature with time evolution upon the ISC are well depicted in Fig. 1.

For the 5% SOC cell (Fig. 4a), after the contact of the steel ball with the pouch wall, the force was increased continuously up to about 282 N at $t = 66$ s, at which point the force drastically dropped to about 21 N accompanied by the indicated voltage drop, revealing the point of internal short related discharge of the cell. The force rose again as the steel ball was continuously pushed against the electrode assembly. Regardless of the force change, the cell voltage continuously decreased and levelled off at 0.4 V. During the internal short, the cell temperature rose by 11 °C. Thus, the thermal runaway is not triggered in this case, but rather the cell's electrochemical discharging dominates the entire process.

However, for the cell with SOC = 60%, several voltage drops and recoveries (5 downward spikes) are observed in Fig. 4b. Eventually, the cell voltage drops to zero. During this process the voltage drop is always accompanied by a drop in the force and an increase in the temperature.

In the high SOC case, *i.e.*, SOC = 95%, the cell voltage exhibits four key response points in time (Fig. 4c and Video 1†): At Point A the cell voltage drops to a low value as the force drops; at Point B the cell voltage fluctuates near the indicated value for about 3 seconds, accompanied by smoke; at Point C the cell voltage falls sharply to zero with a breakout of fire; at Point D the cell burns violently and produces a significant amount of heat. We surmise that at Point A thermal softening of battery components led to the force drop. Starting from Point B, the battery electrochemical process dominates the process early on (the temperatures are lower than 200 °C). As the temperature rises, the chemical reactions gradually dominate the failure evolution behaviour until Point C is reached. The cell temperature then increases sharply to ~650 °C shortly after Point D is reached, *i.e.*, corresponding to the thermal runaway.

Internal material deformation and electrical behaviour of the LIB cells subjected to ball indentation are difficult to characterize *in situ*; therefore, we developed two detailed computational models to reveal the mechanical mechanism driving the ISC trigger event and the subsequent diffusion process leading to a short-circuit. The deformation and fracture of each component are computed using a detailed mechanical finite element (FE) model that takes account of the cover, anode, cathode, separator, and current collector (Simulation methods section and Section 3 of the Extended Data†). In a corresponding manner, the complicated electrochemical behaviour is predicted through a rational framework computational method. Sub-models (*i.e.*, a battery model, a mechanical model, an ISC

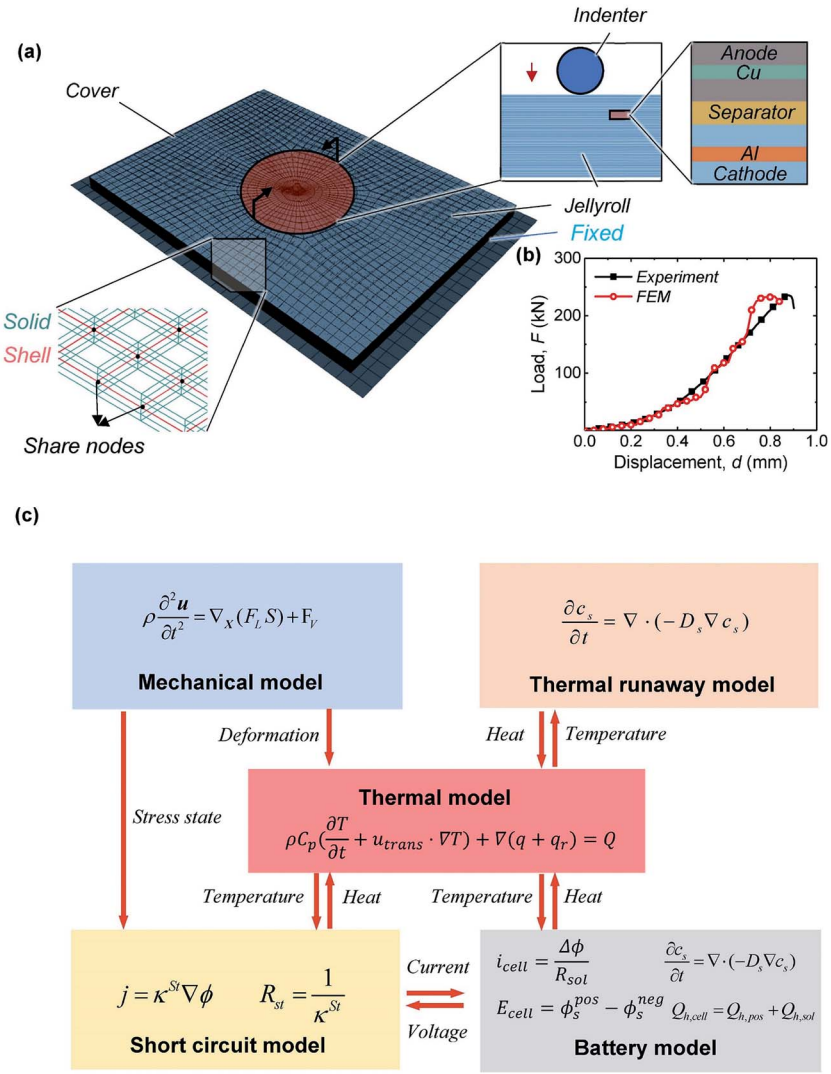

Fig. 3 (a) FEM model of the LIB, detailed mesh and modeling method. (b) Mechanical verification: particle (2 mm) penetration of the LIB. (c) Coupling method and schematic algorithms for the models.

model, a thermal model, and a thermal runaway model) are proposed to account for each critical milestone event during ball penetration. Among them, the mechanical model is used for the loading process before the ISC; the battery model and the ISC model are used together to describe the electrochemical behaviour during the ISC; and the thermal runaway model serves to depict the thermal runaway behaviour. The four mentioned sub-models are coupled with the thermal model. (Detailed information about the modelling can be found in the Simulation methods section and Section 4 of the Extended Data†)

Taking the cell with SOC = 60% as an example, at Point 1 in Fig. 5a no change in the voltage drop and the load drop is observed during the experiment. However, current collector failure occurs before Point 1, as evidenced by the simulation results (Fig. 5a). At Point 2, it is clear that a small voltage drop (~12 mV) started earlier than the force drop indicating that a Ca–An direct touching happens due to failure of the separator. This form of contact corresponds to a larger ISC resistance, based on experiment we performed to calibrate the resistances of all four available ISC types, *i.e.*: (I) An (anode)–Ca (cathode), (II) Ca–Cu (Cu anode collector), (III) An–Al (Al cathode collector), and (IV) Al–Cu (Extended Data Fig. S3†). At Point 3, the cell voltage and load drop simultaneously due to the fracture of cathode active materials (Fig. 5a), leading to a smaller ISC resistance and a larger discharge current. Once the ISC evolved into Point 4 status, anode active materials failed (Fig. 5a) and sparked the Al–Cu type ISC with an extremely small resistance (Extended Data Fig. S3†). With the aid of the computational model, we can vividly observe the progressive (Point 1 to Point 4) failure of the current collector, separator, anode, and cathode with increasing ball penetration.

An ISC cell can be regarded as a complete circuit by itself wherein the internal resistance and ISC resistance are in series. Thus, the resistance change is responsible for the sudden drop of the measured voltage. Two typical voltage drop responses were extracted from the experimental results: a slight drop (*e.g.* Point 2 to Point 3 in Fig. 5a) due to the large contact resistance

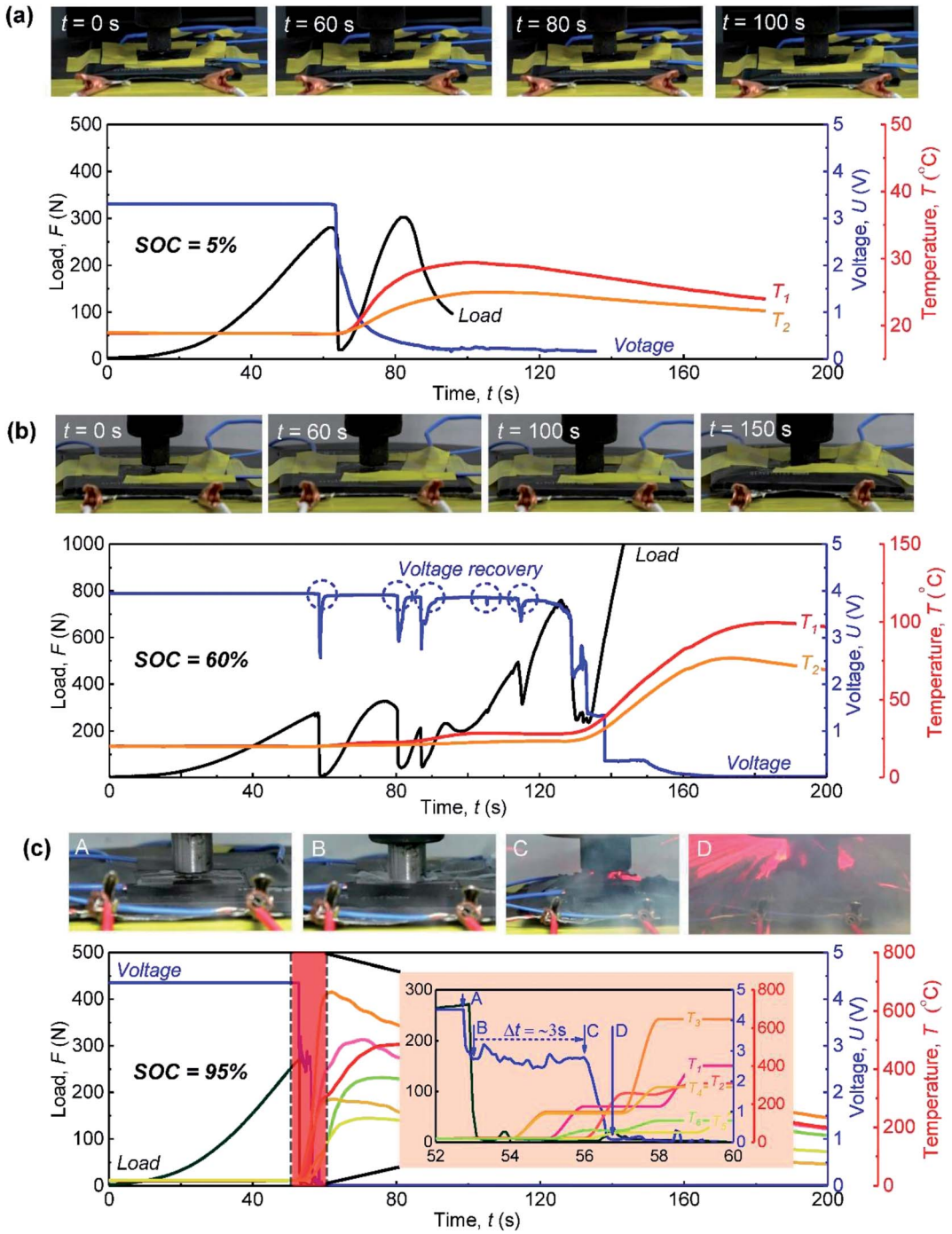

Fig. 4 Load–, voltage and temperature–time curves for batteries at different SOC values, including (a) low SOC (5%), (b) medium SOC (60%) and (c) high SOC (95%), after a foreign body (a 2 mm-diameter ball) was pressed into the cells at a speed of 1 mm min^{-1}.

produced by the contact of the positive and negative electrodes without the Al–Cu contact (*i.e.*, minor ISC, case 1) and a sharp drop (*e.g.*, Point 3 in Fig. 5a) caused by the direct Al–Cu contact (*i.e.*, resulting in a major ISC, case 2).

Through simulation, we predict two types of failure modes after point 1, *i.e.* case 1 and case 2 (Fig. 5a). Case 1 is the same as discussed above (Fig. 5a). For case 2, the major ISC initiates directly and earlier than Case 1 perhaps because the fractured current collector produces some sharp tips that penetrate the separator and electrode active materials leading to an Al–Cu contact. The randomness is believed to be caused by the failure of the current collector and roughness of the edge shape.

We surmise that once the major ISC is triggered, there are three typical modes of ISC evolution in our designed experiments. Mode I represents the voltage drop to a significantly lower value with a plateau, and then subsequently a further drop to 0 in high SOC cells. Mode II denotes the voltage drop to a low value and then recovery to a stable value (smaller than the

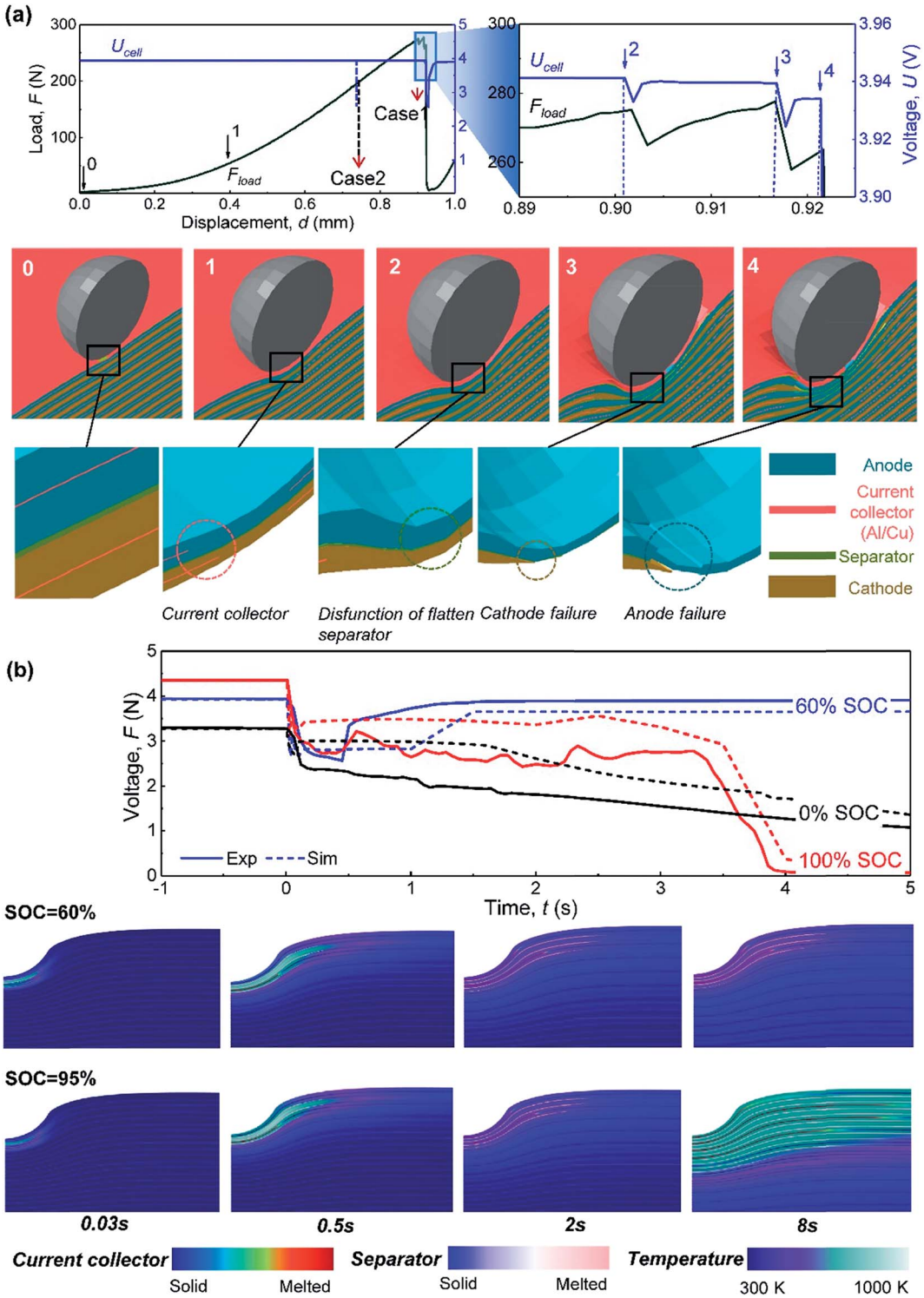

Fig. 5 Utilized simulated analysis to demonstrate the mechanism of the electrical behaviour of an LIB: (a) during penetration before a major ISC (FE model) and (b) during penetration after a major ISC (sub-models).

original voltage) in medium SOC cells, and Mode III refers to the voltage drop to a low value followed by a gradual drain to 0 in low SOC cells. The simulations from the sub-models replicate the trends for all three modes of the experiments as shown in Fig. 5b. In part the melting of the separator and current collector both in high/medium SOC cells is replicated as well. The differences are that separator melting stops after 2 s for 60% SOC cells but is extended for 95% SOC cells (Videos 2 and 3†) Those results indicated that the melting of the separator and current collector diffusion determined the evaluation process of

the ISC. Thus, we define a soft ISC as what happens when current collector melting (60% SOC cells for example or no melting in low SOC cells) is dominant, while a hard ISC happens when separator melting is dominant (95% SOC cells for example).

Based on the observed experimental phenomena and mechanism analysis, Fig. 6a summarizes the mechanical load induced cell failure mode and corresponding thermal behaviour. Fundamentally, the stress governs the triggering of different ISC types (minor ISC/major ISC) where the mechanical failure of separator, cathode, and anode may trigger and/or cause a combination of different ISC modes. With the evolution of stress upon the indention loading, the current collector fails leading to a separator dis-function, such as, to trigger the Ca–An mode ISC. At that time, a minor voltage drop occurs (*i.e.*, minor ISC). As the indentation proceeds, the electrodes fail and cause the Cu–Al mode ISC with an obvious voltage drop (*i.e.*, major ISC). In particular, the features of battery components after the ISC are also shown in Fig. 6b (take SOC = 60% for example). For the minor ISC, we unloaded the cell right after the soft ISC occurred (as evidenced by the drop-in voltage) and immediately disassembled it. Evidence of compressive deformation and a small hole was found in the separator. No significant perforation was detected on the electrode surface but cracks were observed on the edge of the extruded area due to large deformation. Similarly, for the major ISC, which brings with it a voltage drop-recovery situation (Fig. 6b), we also unloaded and disassembled the cell after the onset of the major ISC. In this case, extruded areas of the separator were found to have melted (as shown in the separator related image in Fig. 6b). The local areas beside the extruded point were also melted and consequently cut off the current path to stop further discharging of the cell. This allowed the recovery of voltage to a slightly lower but stable value (Fig. 6b).

Alternatively, the current collector failure may lead to collector tip penetration into the separator and electrode active materials, which can cause a major ISC directly. The starting point for describing the electrochemical behaviour of the cell until now is triggered fully by the mechanical response of the materials. After that, the evolution of the electrochemical response becomes dominant. The onset of the major ISC causes a drastic heat generation leading to an increase in the local temperature, followed by melting of the separator (m.p. = 130 °C) and the current collectors as well (m.p. of Al = ~600 °C, m.p. of copper = ~1100 °C). If the local heat is generated fast enough and the temperature is high enough, more than one component could be melted. The melting behaviour ultimately determines whether the drop in voltage is recoverable (soft ISC) or not (hard ISC). For instance, the drop in voltage of the 60% SOC battery recovered but the 95% SOC battery did not. The local heat

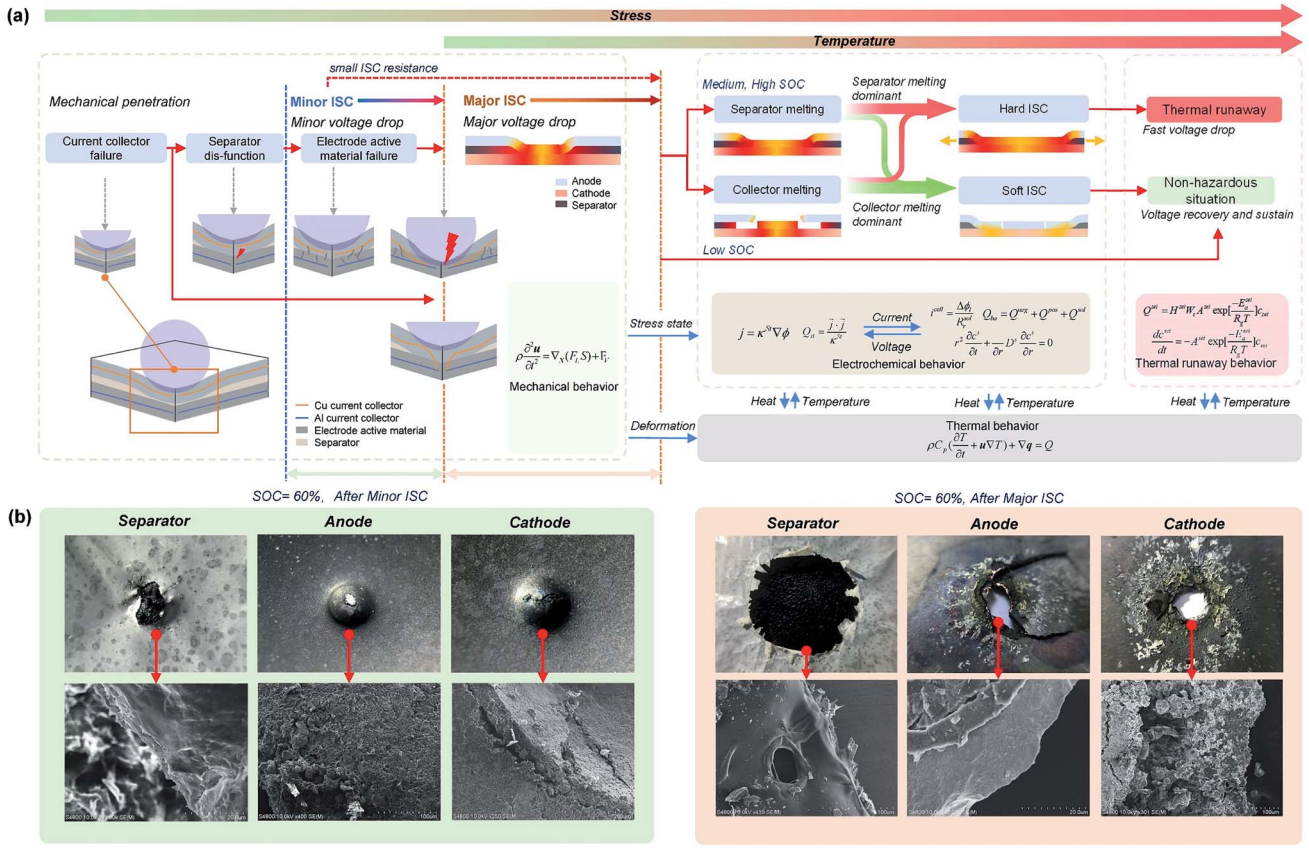

Fig. 6 The electrical behaviour modes and mechanisms of the cells upon mechanical loading. (a) The evaluation from the mechanical loading to thermal runway/non-hazardous situation and principles of multi-field coupling. (b) The characterization of the two ISC types, including the minor ISC (left) and major ISC (right).

melted the collector and cut down the current for the 60% SOC case, while it was too large to make the separator melted area extend rapidly even though the collector was also melted for the 95% SOC case. Thus, the hard ISC occurred when SOC = 95% and the soft ISC occurred when SOC = 60%. In the meantime, the heat of 5% SOC LIB was too low to melt a collector but separator of a local limited area. Once the soft ISC occurs or in a low SOC situation, the cell stays in a non-hazardous state while for the hard ISC case, an inevitable thermal runaway occurs.

Using the computational models, we are capable to investigate the full spectrum of safety behaviours of the lithium-ion cells. The results are summarized in Fig. 7. Intuitively, SOC and resistance should serve as governing factors to determine the safety of a lithium-ion battery after the ISC. Here, SOC, R_r (ISC resistance), and R_rA (product of ISC resistance and contact area) are used as dominant variables. The initial SOC determines the maximum energy released during an ISC. Thus, when the SOC is low enough, the cell will remain safe even if a hard ISC is triggered (the low SOC boundary could be around SOC < 0.2). Based on the contact resistance experiments we discussed above, the initial area resistance (R_rA, if A stays the same, such as in indentation) determines the ISC type. A minor ISC does not include the Cu–Al contact, so R_rA ranges between 122 Ω mm^2 (the minimum value of the Cu–An, Al–Ca and An–Ca contact) and 300 Ω mm^2 (the maximum value of the Cu–An, Al–Ca and An–Ca contact). R_rA values for a major ISC range between 4 Ω mm^2 (the minimum value of the Cu–Al contact) and 50 Ω mm^2 (the maximum value of the Cu–Al contact). In all cases, the resistance is measured with an Agilent 34420A digital voltmeter and the contact area is determined by the indentor contact area. Detailed data are shown in Extended Data Fig. S4e.† Note that if the Cu–Al contact happens, a fusing Al–Cu interface is produced with rising temperature and the electrical resistivity of the Al–Cu contact is drastically reduced to around 45 to 85 μΩ cm.[29] Clearly, more initial ISC heat will be produced when R_rA is smaller.

In the minor ISC zone it is still possible for a thermal runaway to be directly triggered if the contact area is large enough (not observed in our experiments due to constant contact area). The major ISC zone may be divided into 4 types as illustrated in Fig. 7A and is a soft ISC with insufficient heat to cause separator melting; Fig. 7B and D illustrate hard ISCs dominated by separator melting; Fig. 7C illustrates a soft ISC with current collector melting. The two hard ISC types are both caused by separator melting. This evolution map gives us comprehensive insights into LIB safety evaluation after an ISC is triggered.

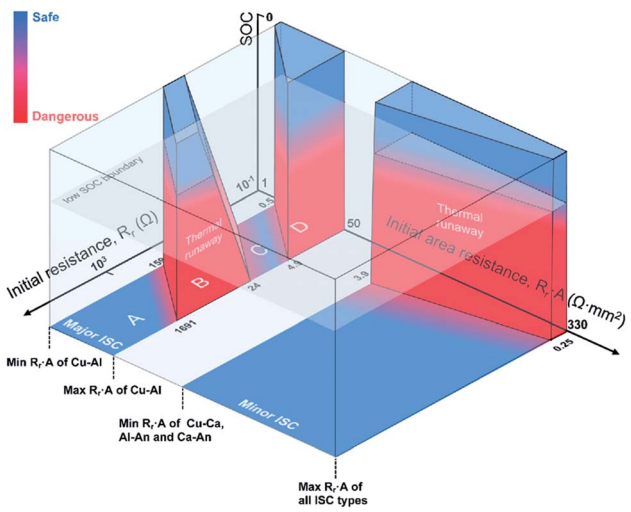

Fig. 7 The safety boundary of the LIB after an internal short circuit based on the multi-physics model. The ISC form will be identified by the distribution of R_rA – axial value: 5 Ω mm^2 ~ 50 Ω mm^2 for major ISC cases and 122 Ω mm^2 and 300 Ω mm^2 for minor ISC cases. R_rA, R_r and SOC together determine the extent of the danger.

5. Conclusions

In summary, we have discovered different electrochemical behaviours of a lithium-ion cell upon the initiation of an ISC using a highly reproducible mechanical penetration method. Multi-physics computational models and physical tests prove that mechanical deformation, stress distribution, and failure processes acting together determine the particular mode(s) of the ISC, such that voltage change and temperature rise may lead to different levels of safety performance for LIBs. A full spectrum safety mechanism map is developed that should provide useful fundamental guidance for lithium-ion battery safety design, evaluation, prediction, and protection.

Author contributions

J. X. and Y. L. developed the concept and designed the study; J. X. and Y. L. supervised the project. B. L., Y. J., and J. L. designed and conducted the experiments; B. L. and Y. J. conducted part of the numerical simulation work; S. Y., C. Y. and Z. H. contributed to the numerical simulation work. All authors contributed to the development of the manuscript and discussions as the project developed.

Conflicts of interest

There are no conflicts to declare.

Acknowledgements

This work is financially supported by the National Science Foundation of China (11872099), the National Key Research and Development Program of China (2017YFB0103703), the research Project of the State Key Laboratory of Vehicle NVH and Safety Technology under Grant NVHSKL-201610, and the Opening project of State Key Laboratory of Explosion Science and Technology (Beijing Institute of Technology) with the project number KFJJ17-13M.

References

1 C. Y. Wang, G. S. Zhang, S. H. Ge, T. Xu, Y. Ji, X. G. Yang and Y. J. Leng, *Nature*, 2016, **529**, 515–518.
2 J. Lu, Y. J. Lee, X. Y. Luo, K. C. Lau, M. Asadi, H. H. Wang, S. Brombosz, J. G. Wen, D. Y. Zhai, Z. H. Chen, D. J. Miller, Y. S. Jeong, J. B. Park, Z. Z. Fang, B. Kumar, A. Salehi-Khojin, Y. K. Sun, L. A. Curtiss and K. Amine, *Nature*, 2016, **529**, 377–382.
3 K. Bourzac, *Nature*, 2015, **526**, S105.
4 L. W. Ji, Z. Lin, M. Alcoutlabi and X. W. Zhang, *Energy Environ. Sci.*, 2011, **4**, 2682–2699.
5 V. Etacheri, R. Marom, R. Elazari, G. Salitra and D. Aurbach, *Energy Environ. Sci.*, 2011, **4**, 3243–3262.
6 O. K. Park, Y. Cho, S. Lee, H. C. Yoo, H. K. Song and J. Cho, *Energy Environ. Sci.*, 2011, **4**, 1621–1633.
7 M. Keyser, D. Long, Y. S. Jung, A. Pesaran, E. Darcy, B. Mccarthy, L. Patrick and C. Kruger, *Development of a Novel Test Method for On-Demand Internal Short Circuit in a Li-Ion Cell*, Pasadena, California, 2011.
8 D. P. Finegan, E. Darcy, M. Keyser, B. Tjaden, T. M. M. Heenan, R. Jervis, J. J. Bailey, R. Malik, N. T. Vo, O. V. Magdysyuk, R. Atwood, M. Drakopoulos, M. DiMichiel, A. Rack, G. Hinds, D. J. L. Brett and P. R. Shearing, *Energy Environ. Sci.*, 2017, **10**, 1377–1388.
9 M. T. F. Rodrigues, G. Babu, H. Gullapalli, K. Kalaga, F. N. Sayed, K. Kato, J. Joyner and P. M. Ajayan, *Nat. Energy*, 2017, **2**, 17108.
10 K. Liu, W. Liu, Y. C. Qiu, B. A. Kong, Y. M. Sun, Z. Chen, D. Zhuo, D. C. Lin and Y. Cui, *Sci. Adv.*, 2017, **3**, 8.
11 D. Ren, X. Feng, L. Lu, M. Ouyang, S. Zheng, J. Li and X. He, *J. Power Sources*, 2017, **364**, 328–340.
12 Y. Z. Li, Y. B. Li, A. L. Pei, K. Yan, Y. M. Sun, C. L. Wu, L. M. Joubert, R. Chin, A. L. Koh, Y. Yu, J. Perrino, B. Butz, S. Chu and Y. Cui, *Science*, 2017, **358**, 506–510.
13 H. Wu, D. Zhuo, D. S. Kong and Y. Cui, *Nat. Commun.*, 2014, **5**, 6.
14 P. Bai, J. Li, F. R. Brushett and M. Z. Bazant, *Energy Environ. Sci.*, 2016, **9**, 3221–3229.
15 B. Liu, H. Zhao, H. Yu, J. Li and J. Xu, *Electrochim. Acta*, 2017, **256**, 172–184.
16 B. Liu, S. Yin and J. Xu, *Appl. Energy*, 2016, **183**, 278–289.
17 C. Zhang, S. Santhanagopalan, M. A. Sprague and A. A. Pesaran, *J. Power Sources*, 2015, **290**, 102–113.
18 S. Santhanagopalan, P. Ramadass and J. Zhang, *J. Power Sources*, 2009, **194**, 550–557.
19 D. P. Finegan, M. Scheel, J. B. Robinson, B. Tjaden, I. Hunt, T. J. Mason, J. Millichamp, M. Di Michiel, G. J. Offer, G. Hinds, D. J. L. Brett and P. R. Shearing, *Nat. Commun.*, 2015, **6**, 6924.
20 Z. H. Chen, Y. Qin, Y. Ren, W. Q. Lu, C. Orendorff, E. P. Roth and K. Amine, *Energy Environ. Sci.*, 2011, **4**, 4023–4030.
21 M. X. Zhang, J. Y. Du, L. S. Liu, A. Stefanopoulou, J. Siegel, L. G. Lu, X. M. He, X. Y. Xie and M. G. Ouyang, *J. Electrochem. Soc.*, 2017, **164**, A3038–A3044.
22 C. J. Orendorff, E. P. Roth and G. Nagasubramanian, *J. Power Sources*, 2011, **196**, 6554–6558.
23 R. Zhao, J. Liu and J. J. Gu, *Energy*, 2017, **123**, 392–401.
24 W. Fang, P. Ramadass and Z. Zhang, *J. Power Sources*, 2014, **248**, 1090–1098.
25 P. Ramadass, W. Fang and Z. Zhang, *J. Power Sources*, 2014, **248**, 769–776.
26 T. Volck, W. Sinz, G. Gstrein, C. Breitfuss, S. Heindl, H. Steffan, S. Freunberger, M. Wilkening, M. Uitz and C. Fink, *Batteries*, 2016, **2**, 8.
27 M. X. Zhang, L. S. Liu, A. Stefanopoulou, J. Siegel, L. G. Lu, X. M. He and M. G. Ouyang, *J. Electrochem. Soc.*, 2017, **164**, A2738–A2745.
28 K.-C. Chiu, C.-H. Lin, S.-F. Yeh, Y.-H. Lin and K.-C. Chen, *J. Power Sources*, 2014, **251**, 254–263.
29 W.-B. Lee, K.-S. Bang and S.-B. Jung, *J. Alloys Compd.*, 2005, **390**, 212–219.